

Chapter 4

Shear Stress Imager

The active control of turbulent flows has long been a dream of fluid mechanists because of its potential impact on the aerospace industry [1,2,3]. Up to now, however, little has been done mainly because of the unavailability of miniature devices whose sizes are comparable to the feature sizes in high-Reynolds-number turbulent flows. Among these previously unavailable devices are the distributed shear stress sensor arrays. They are responsible for the real-time collection of wall shear stress information, which is processed by detection circuits to identify the turbulence structure. This chapter describes the development of such a shear stress imager using the shear stress sensor developed in Chapter 3 and its shear stress profiling capability in turbulent boundary layers.

4.1 Turbulent Boundary Layer and Streamwise Vortices

The basic understanding of turbulent boundary layer and vortex structure is important for the proper design of the shear stress imager. Here we only discuss the wall-bound channel flow which will be used for shear stress imaging.

4.1.1 Channel Flow

Figure 4.1 shows the successive stages of development of the boundary layer of an incompressible viscous fluid in a channel, assuming the no-slip boundary condition, i.e., the fluid on the wall is not moving. At the entrance of the channel, uniform flow at free-stream velocity exists. As the fluid moves down the channel, shear friction between the fluid and the wall, and between adjacent fluid layers, retards the motion, causing the boundary layer to grow until it is fully developed. From this point on, the velocity profile

remains unchanged. The length required for the flow to become fully developed is known as the *entrance length* x_e . Note that the free stream velocity U_∞ is replaced by the centerline velocity U_c in calculating the Reynolds number in fully developed channel flow.

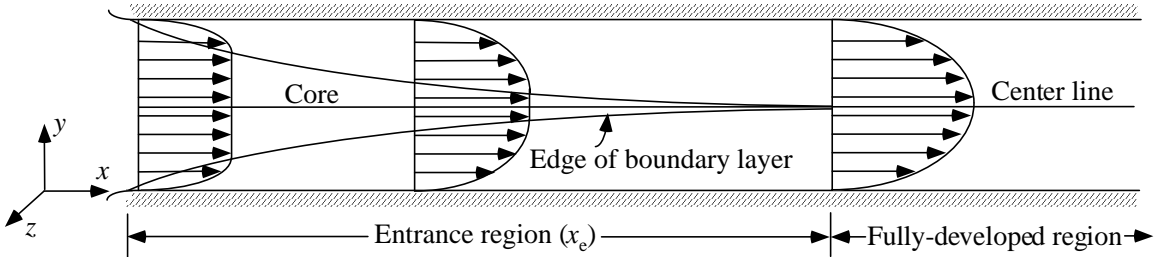


Figure 4.1 Boundary layer development in channel flow.

4.1.2 Wind Tunnel

The wind tunnel that is used in most of the turbulent boundary layer studies is in the UCLA Fluid Mechanics Laboratory. It is 4.87 m long, 60 cm wide and 2.54 cm high. Note that a wind tunnel with this high aspect ratio cross section supplies a two-dimensional channel flow. The walls of the channel are constructed of 2.5 cm thick Plexiglass and supported by a steel frame. An axial blower powered by a DC source supplies the air flow in the channel. At the highest blower speed, the centerline velocity in the channel is about 25 m/s. Hot-wire velocity measurements at 8 m/s indicate that the channel consists of a laminar entrance flow region which gradually transforms into a fully-developed turbulent flow in the downstream 2/3 portion of the channel. All calibration and testing of shear stress sensors and shear stress imaging is carried out in this region of the channel.

In the fully developed region, the mean shear stress is uniform everywhere on the wall because the velocity profiles remains unchanged. A simple force balance on a rectangular control volume of length L , width W and height H gives

$$\tau_w = \frac{H}{2L} \Delta p \quad (4.1)$$

if $W \gg H$, i.e., for a 2-D channel. In the above equation, τ and Δp are the mean shear stress and mean pressure difference. Therefore, the mean shear stress in the 2-D fully developed channel flow can be determined through the measurement of the pressure gradient.

On the other hand, wall shear stress can be expressed as

$$\tau_w = \rho_f u_\tau^2 \quad (4.2)$$

where u_τ is called the *friction velocity* and ρ_f is the density of the fluid. For air at room temperature, ρ_f is 1.21 kg/m^3 . According to [4], the friction velocity is related to the centerline stream velocity and Reynolds number by

$$\frac{u_\tau}{U_c} = 0.119 \text{Re}^{-0.089} \quad (4.3)$$

Here the half height of the wind tunnel $H/2$, i.e., the boundary thickness, is taken as the characteristic length of the Reynolds number. Therefore, the shear stress can also be calculated from the measurement of the free stream velocity from

$$\tau_w = 0.00427 U_c^{1.822} \quad (4.4)$$

It is found that the wall shear stresses determined by the above two methods in our wind tunnel give almost identical results.

4.1.3 Streamwise Vortices and Sub-Layer Structures

It has been revealed that turbulent flow has dual features, deterministic and random. The deterministic part of the turbulence is responsible for most of the mass and momentum transfers for both free and wall-bounded flows [5,6,7]. For wall-bounded channel flow, the quasi-deterministic structures have been numerically and experimentally identified in the fully developed turbulent region to be a pair of counter-rotating streamwise vortices (Figure 4.2). These vortices, which appear randomly in both space and time, bring high velocity fluids down to the wall and create a streak of high

shear stress in the region between the vortices. These streaky structures can be detected through the measurement of near wall velocity [8] or wall shear stress distribution.

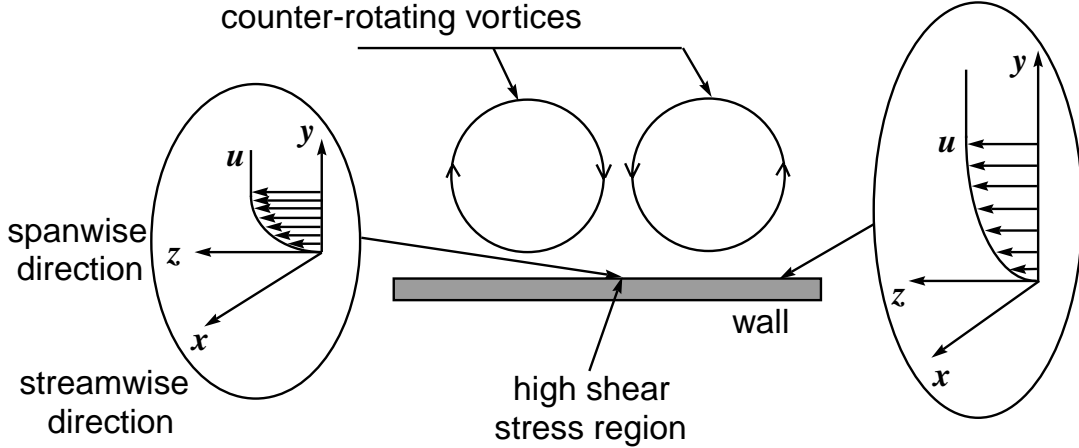


Figure 4.2 Counter-rotating vortex pair.

The statistical sizes of the streaky structures have been reported by a number of authors [9,10,11,12,13,14,15]. Most observed quantities exhibit significant variations. Nevertheless, these are helpful to the design of our shear stress imaging chip. According to Cantwell [5], the thickness of the viscous sub-layer is $7v/u_\tau$; the length of sub-layer structure in the streamwise direction λ_x varies from $100v/u_\tau$ to $2000v/u_\tau$ with $1000v/u_\tau$ as the best value; the vertical half scale of the sub-layer structure λ_y varies from $10v/u_\tau$ to $25v/u_\tau$ with $15v/u_\tau$ as the best value; the spanwise scale of the sub-layer structure λ_z is generally agreed to be $100v/u_\tau$. Here v/u_τ is the viscous length. It decreases as the Reynolds number increases. For the centerline air flow velocity ranging from 8 m/s to 25 m/s in our wind tunnel, the friction velocity u_τ is from 0.394 m/s to 1.111 m/s and the Reynolds number is from 6790 to 21200. The best estimation of the scales of the sub-layer streaky structures corresponding to above flow velocity range is

$$\text{Streamwise scale } \lambda_x = 1000 v/u_\tau = 1.35 \text{ cm} - 3.80 \text{ cm}$$

$$\text{Spanwise scale } \lambda_z = 100 v/u_\tau = 1.35 \text{ mm} - 3.80 \text{ mm}$$

$$\text{Vertical half scale } \lambda_y = 15 v/u_\tau = 0.20 \text{ mm} - 0.57 \text{ mm}$$

These numbers tell us that in order to capture the sub-layer structures (minimum of three sensors per structure) in our wind tunnel, the sensor dimension and spacing of the shear stress imager has to be less than half a millimeter. Traditional flush-mounted hot-film sensors obviously do not meet this dimensional requirement. This is probably one of the reasons why there has been no report on sub-layer structure detection at high Reynolds number.

4.2 Shear Stress Imager

Based on the understanding of the sub-layer streaky structures in turbulent flows, we have developed the $2.85\text{ cm} \times 1.0\text{ cm}$ shear stress imaging chip shown in Figure 4.3 using the $3\text{ }\mu\text{m}$ wide and $150\text{ }\mu\text{m}$ long micro shear stress sensor described in Chapter 3. The chip is specifically designed for the study in turbulent flow with Reynolds number around 10^4 . There are two identical rows of sensors 5 mm apart and normal to the streamwise direction. This streamwise pitch is chosen such that at least three data points can be taken from a streak in the streamwise direction. Each row has 25 sensors with $300\text{ }\mu\text{m}$ pitch, which is already the minimum for this type of sensor. It should give at least three data points from a streak in the spanwise direction and be able to catch more than one streak. Between the two major rows of sensors, there are two 5-sensor rows and one 25-sensor row for the detection of streak details in spanwise direction. The 1 cm spacing between the sensors and the bonding pads on the left and right edges of the chip is necessary to avoid the upstream bonding wires from interfering with the downstream sensors.

The fabrication process of the shear stress imager is basically the same as that of a single sensor but it needs two more masks for the final metallization step. The yield of sensors on a imaging chip is important even for laboratory testing purpose. Thanks to the well-designed process, more than 95% of the sensors on each chip can be used for measurement.

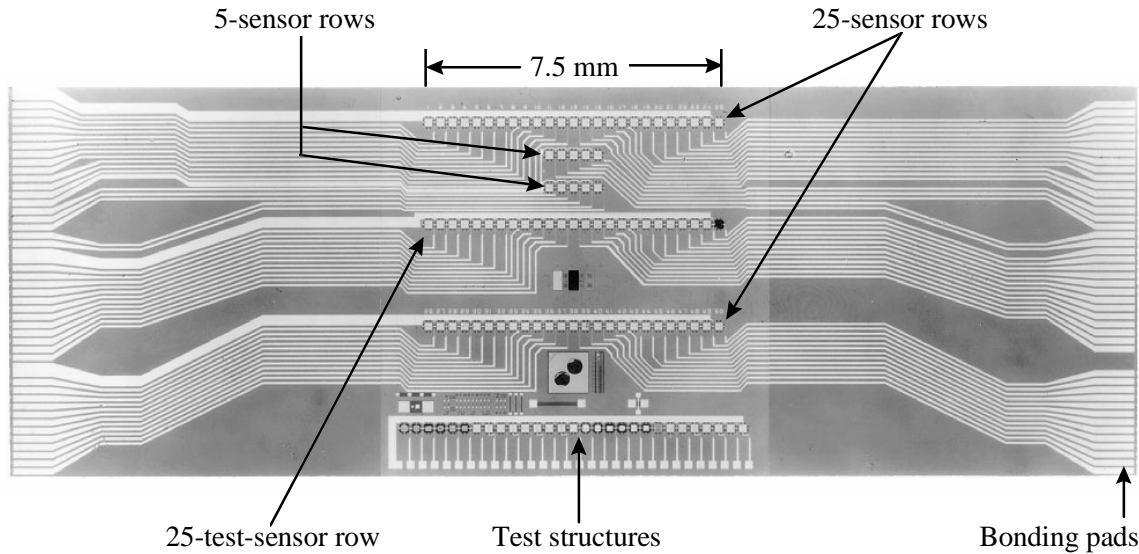


Figure 4.3 The micromachined shear stress imager ($2.85 \times 1 \text{ cm}^2$) with over 100 sensors.

4.3 Packaging, Biasing and Calibration

The package for the imaging chip is a fine-line PC board with a chip-size recess in the center so that the imaging chip can be flush-mounted. The chip and the PC board are electrically connected by wire bonding (Figure 4.4). The electrical leads are soldered on the backside of the PC board. The PC board is then flush-mounted on a specially-made plug which fits into the wall of the wind-tunnel (Figure 4.5), with the sensor row perpendicular to the flow direction.

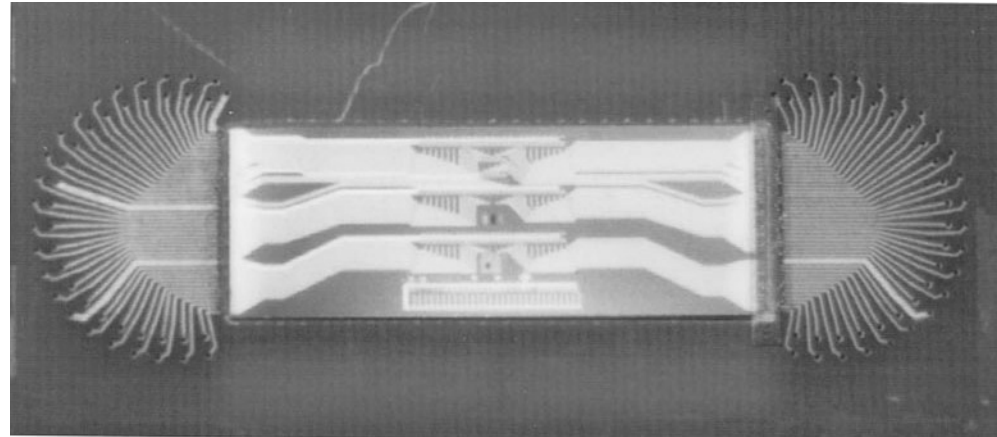


Figure 4.4 Photograph of the packaged shear stress imager.

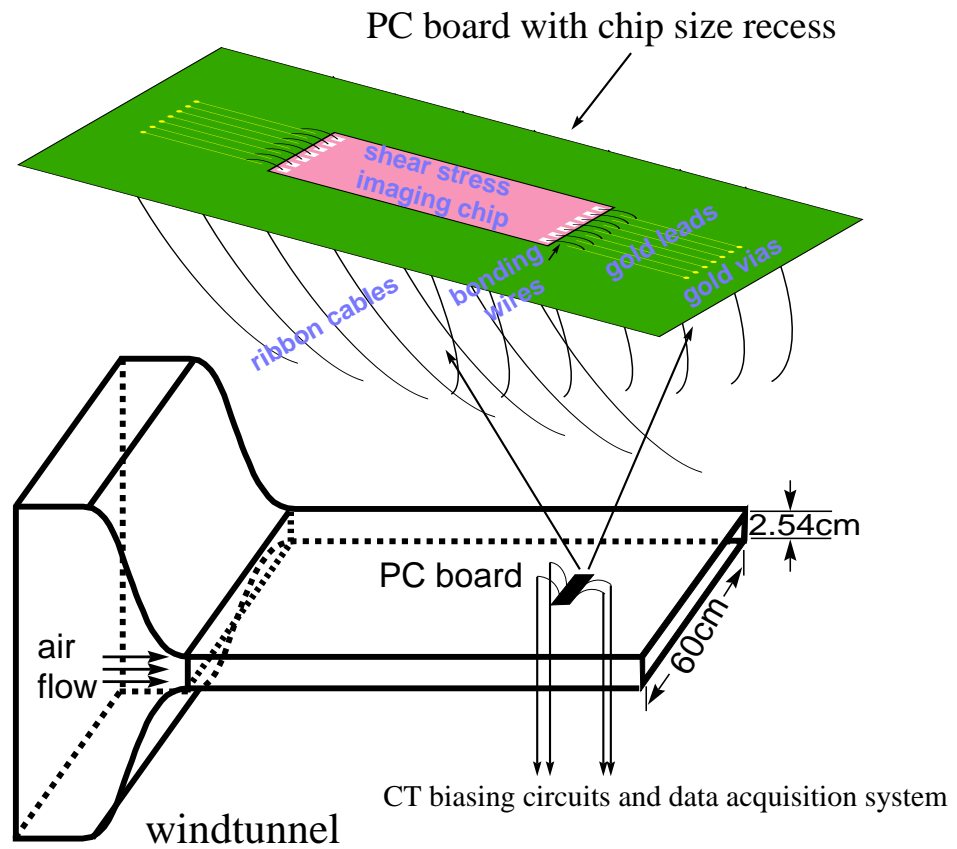
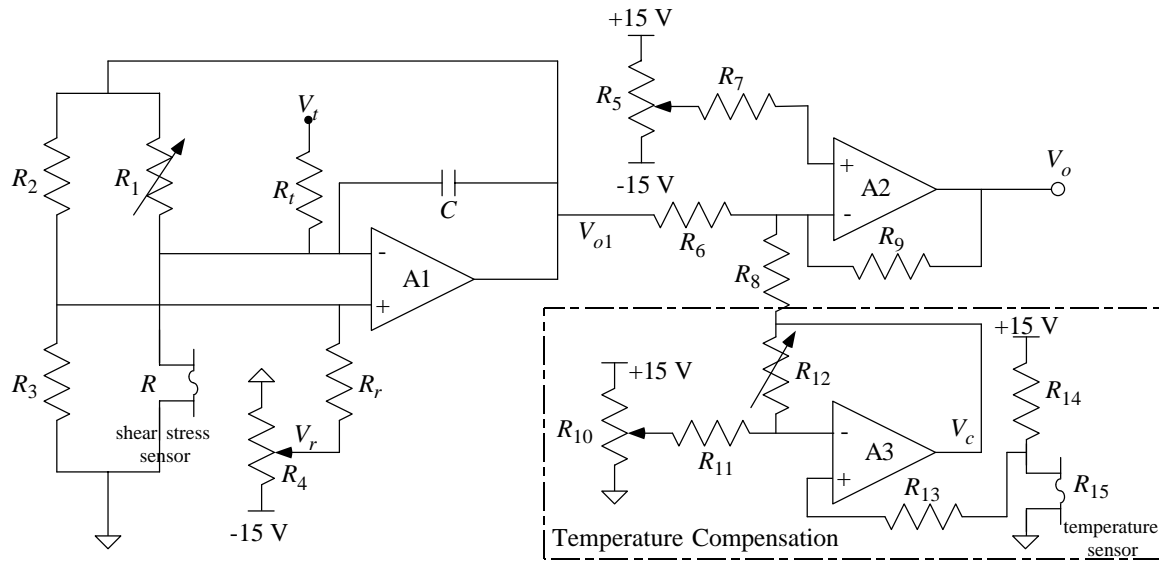


Figure 4.5 Imaging chip package and wind tunnel setup.

In our experiments, the sensors are biased in constant temperature (CT) mode. Although it is more complicated than the constant current mode, it can achieve much higher frequency bandwidth which is crucial in turbulence measurement. Therefore, arrays of CT circuits and gain stages have been made on PC boards using op-amps and other discrete components (Figure 4.6). The dc offset of the outputs can be adjusted individually, but the gain is fixed to be 10. A computer-controlled data acquisition system is used to measure all the outputs simultaneously.



A_1, A_2, A_3 : OP-27

$R_3 = R_3/a_R$ (a_R : over-heat ratio)

$C = 100-500\text{ pF}$

R_1 : 3.6 k Ω multi-turn precision potentiometer

$R_2 = R_3 = R_6 = R_7 = R_8 = R_{11} = R_{13} = 5.0\text{ k}\Omega$

R_{15} : temperature sensor - shear stress sensor operated at very low power

Temperature compensation stage can be shared by all channels

R_4, R_5 and R_{10} : 10 k Ω multi-turn pots

$R_r = R_t = 1\text{ M}\Omega$

$R_9 = 50\text{ k}\Omega$

R_{12} : 470 k Ω multi-turn precision pot

$R_{14} = 150\text{ k}\Omega$

Figure 4.6 Constant temperature biasing circuit, gain stage and temperature compensation stage.

Before the sensors are used to measure the shear stress distribution, their dc outputs are calibrated against known wall shear stress levels which are calculated from the centerline velocity by using Eq. (4.4). Figure 4.7 shows the calibration results for 10

sensors in a row. Although each sensor has different offset, the trend of all curves are almost the same. Polynomial fitting is performed on each curve to extract the fitting parameters for later use in real data processing.

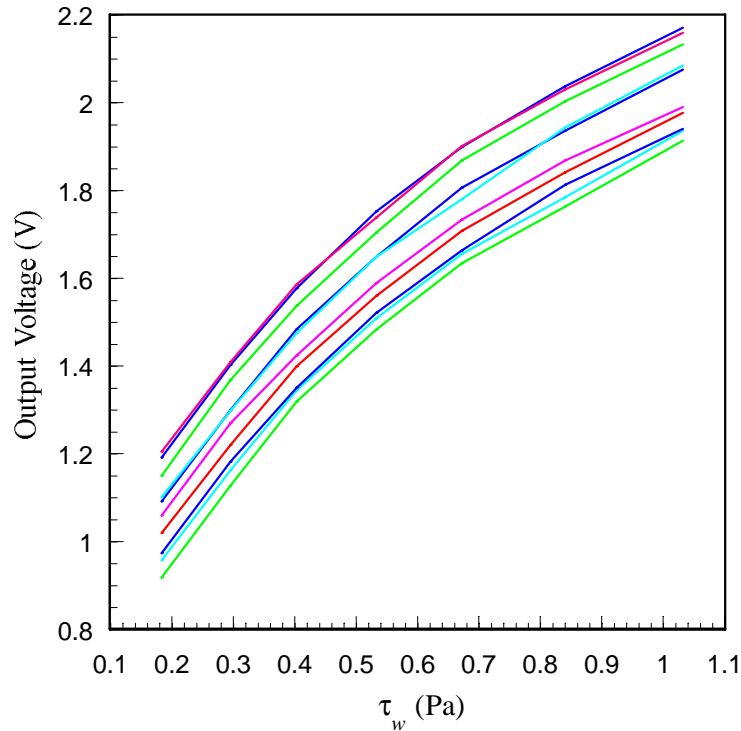


Figure 4.7 Calibration curves of 10 sensors in a row.

The temperature of the air flow in the wind tunnel is not a constant because of the warm-up of the blower and the fluctuating ambient temperature. The maximum flow temperature change can be as high as 5°C. On the other hand, the shear stress sensors have temperature sensitivities in the order of -(150-200) mV/°C (after gain of 10) around room temperature. Therefore, serious drifts on the DC outputs of the shear stress sensors during the real time data acquisition is expected and could cause the measured data to be useless. There are two ways to compensate for the drifts. The first method is to use the simple temperature compensation circuit in Figure 4.6. Here the temperature sensor can be a shear stress sensor operated at very low power such that the self-heating is negligible. Note that the output of the compensation circuit V_c can be shared by all the

channels so only one such circuit is needed for all the sensors in use. The results in Figure 4.8 show that an order of magnitude of improvement of the thermal stability has been achieved. The other way to compensate the drifts is to do post processing on the data, using the flow temperature history data recorded by a temperature sensor. Both methods requires calibration of the temperature sensitivity for each sensor. Obviously, the first method is suitable for real time measurement and control, but the second one is simpler.

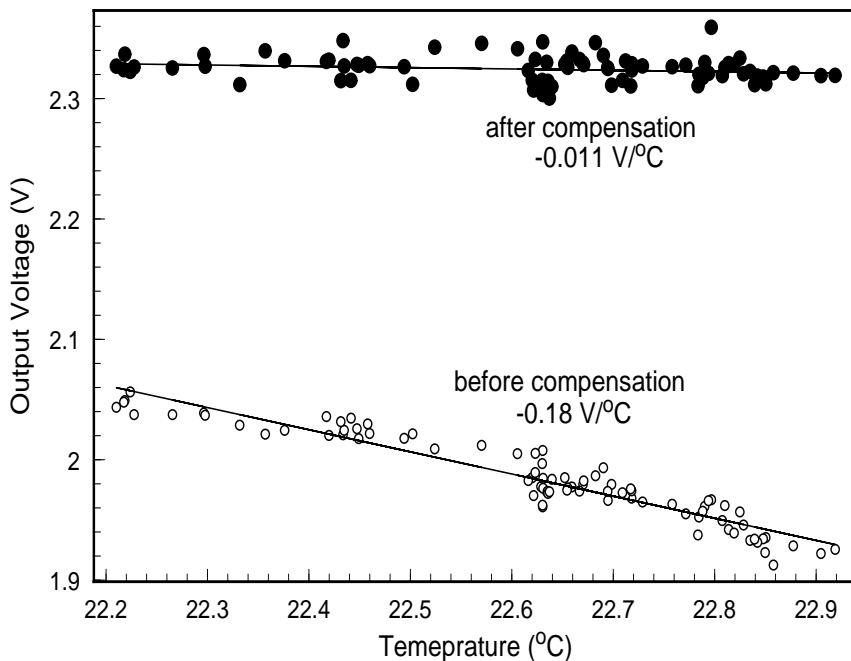
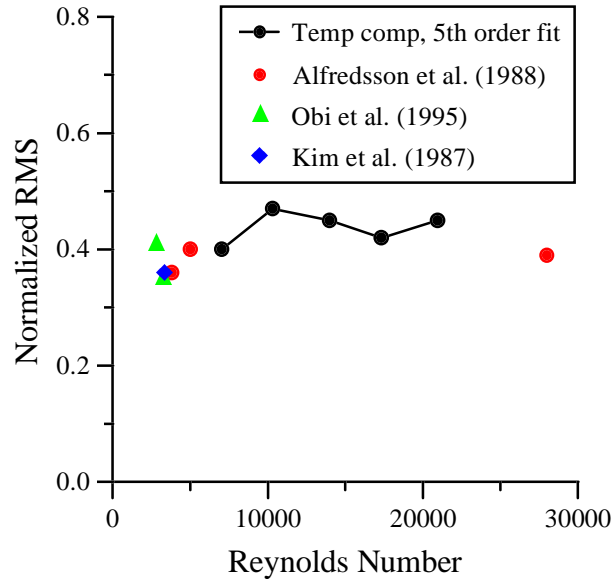


Figure 4.8 Typical temperature sensitivities before and after temperature compensation of a shear stress sensor.

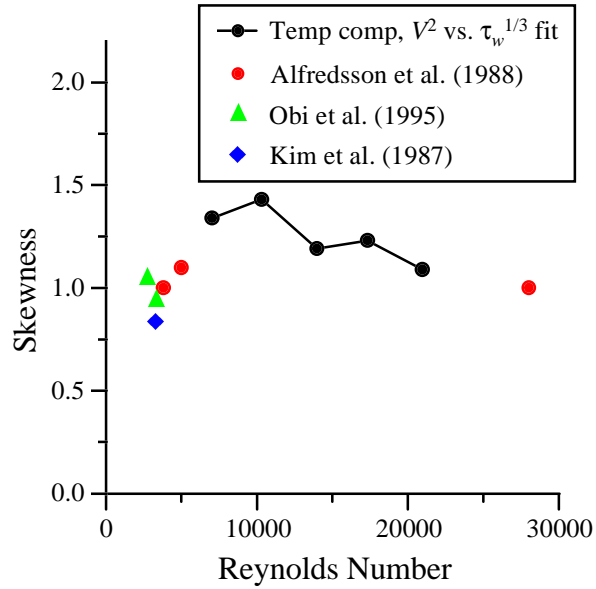
4.4 Shear Stress Imaging

For real-time shear stress imaging, the output voltage is sampled at a rate higher than 10kHz and converted to a shear stress signal based on the calibration performed previously. In order to establish the credibility of the imaging chip, the turbulence statistics calculated from the shear stress fluctuations recorded by a single shear stress sensor are compared to previously established results. Figure 4.9 shows the comparison in

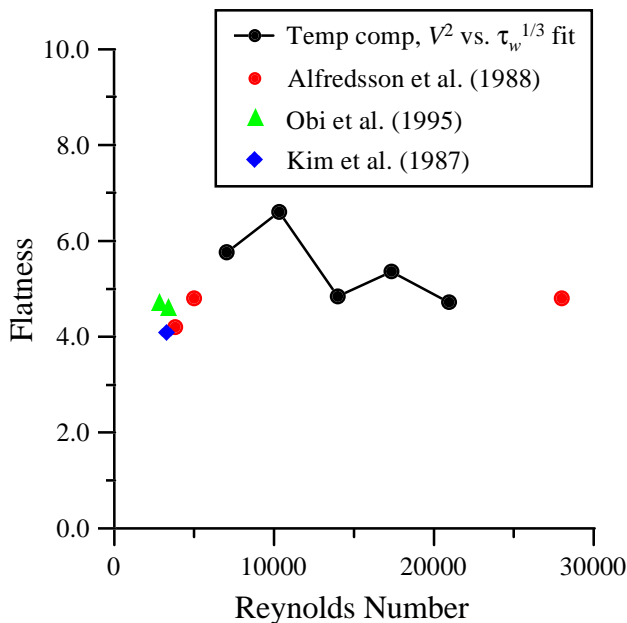
terms of the normalized RMS level, the skewness factor, and the flatness factor. It is obvious that the present results agree very well with previous studies in all three areas [16,17,18]. In addition, the present statistics appear to be independent of the Reynolds number which is predicted by turbulence theory.



(a) RMS values of the shear stress fluctuations normalized to the corresponding DC shear stress.



(b) Skewness factor.



(c) Flatness factor.

Figure 4.9 Turbulence statistics based on the shear stress fluctuations recorded by the micro shear stress sensors on the imaging chip.

Another validation method is to compare the instantaneous output from a shear stress on the flush-mounted imaging chip with that from a hot-wire anemometer directly above the shear stress sensor because near wall hot wire measurement has been considered as one of the standard techniques in the studies of sub-layer structures, although it can only give instantaneous velocity signal at one location. The vertical distance from the hot wire to the wall must be smaller than the vertical half scale ($\lambda_y = 15 v/u_\tau$) of a sub-layer streaky structure so that both the shear stress sensor and the hot wire are within the same structure. The hot wire we used for this test is a 1 mm long platinum wire 2.5 μm in diameter operated in CT mode with a bandwidth of 30 kHz. Its vertical distance from the shear stress sensor is about 0.4 mm, which is equivalent to 12.5 v/u_τ at a centerline velocity of 10 m/s. The measurement results at this velocity are shown in Figure 4.10. It can be seen that the two output traces are very similar, indicating that the flush-mounted shear stress sensor is truly measuring the sub-layer structure as the widely used

conventional hot wires are. The output of the shear stress sensor gives a little more details because it is much shorter than the hot wire.

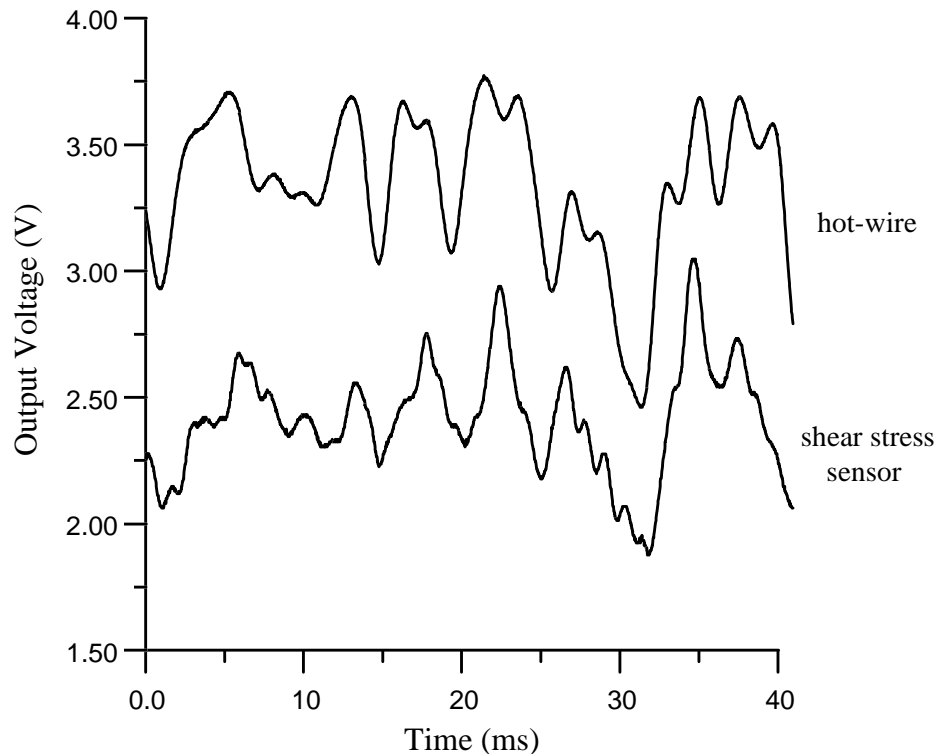


Figure 4.10 Comparison between the instantaneous outputs from a shear stress on the flush-mounted imaging chip and a 1 mm long hot-wire anemometer 0.4 mm above the shear stress sensor at a centerline velocity of 10 m/s.

The instantaneous turbulent shear stress distributions of the channel were recorded by using one of the sensor rows on the imaging chip. Figure 4.11 shows the contour plots of the time evolution of the shear stress distributions at two different centerline velocities. The red streaky structures in the plots represent regions of high shear stress on the wall of the channel where the sensor row is located. They are caused by the presence of near-wall streamwise vortices which bring high momentum fluid from the free stream to the wall. Due to the small-scale nature of these structures, previous experiments in turbulent boundary layers have only succeeded in qualitatively demonstrating their existence

without obtaining any quantitative information. This is the first time that these near-wall structures are quantitatively recorded.

In Figure 4.11, the time axis can be converted to the spatial scale in streamwise direction by multiplying it with the convection velocity U_{con} ($\sim (0.5-0.6)U_c$) so the plots look like 2-D shear stress images. We call them *pseudo* 2-D shear stress distribution plots. They are so named because if the lifetime of the sub-layer structures passing the sensor row is longer than the data-taking time, these plots then represent the instantaneous shear stress distribution of these structures in the vicinity of the sensor row. The above assumption about the lifetime is known as Taylor's hypothesis in fluid mechanics and it holds in most cases.

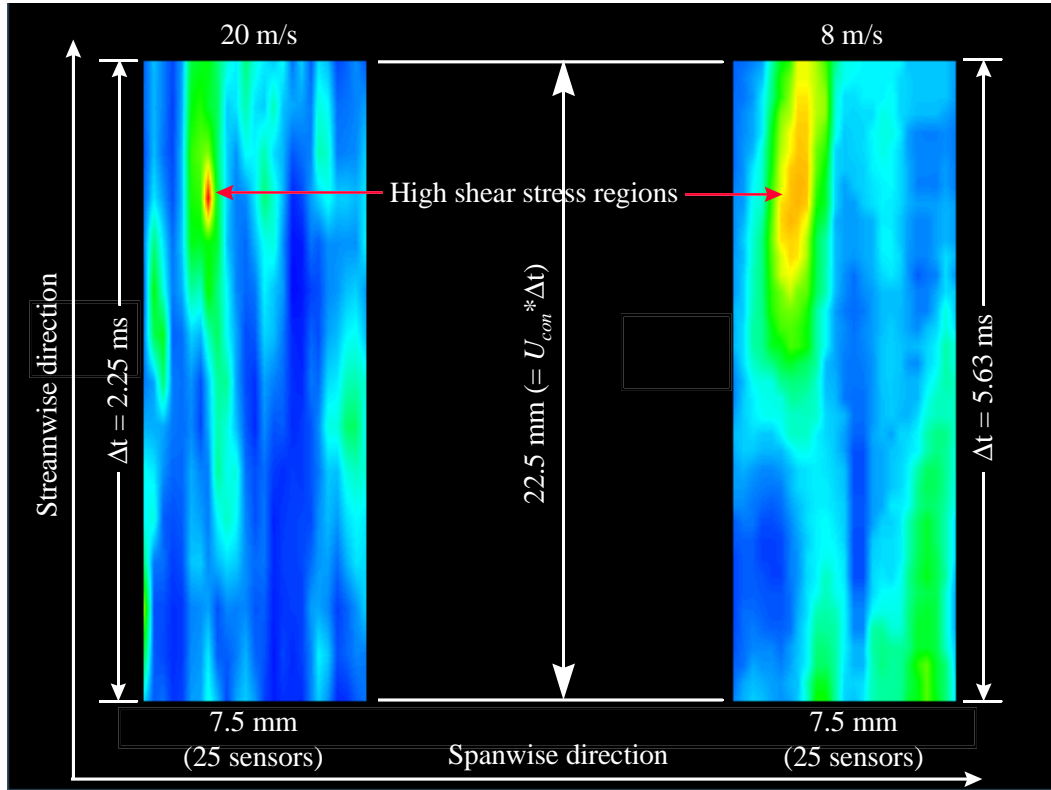


Figure 4.11 Contour plots of the pseudo 2-D shear stress distributions. Red area indicates high shear stress and blue area indicates low stress.

To confirm the validity of the above hypothesis, we have performed the real-time 2-D shear stress imaging for a period of time using the 5×4 sensor array located on the top-middle region of the imaging chip (Figure 4.3). The results are shown in Figure 4.12. On the right is a pseudo 2-D plot generated from the outputs of the 5 sensors on the first row at four different times (0 ms, 0.083 ms, 0.167 ms and 0.25 ms), while on the left is the real 2-D plot generated from the instantaneous outputs of the 5×4 sensor array recorded at the time of 0.25 ms. Note that the top and the bottom of the pseudo plot correspond to the measurements at 0 ms and 0.25 ms respectively. It can be clearly seen that these two plots are showing the same structure. The difference is on the peak shear stress level. We have found that the pseudo 2-D plots always show a lower peak level than the real 2-D plots.

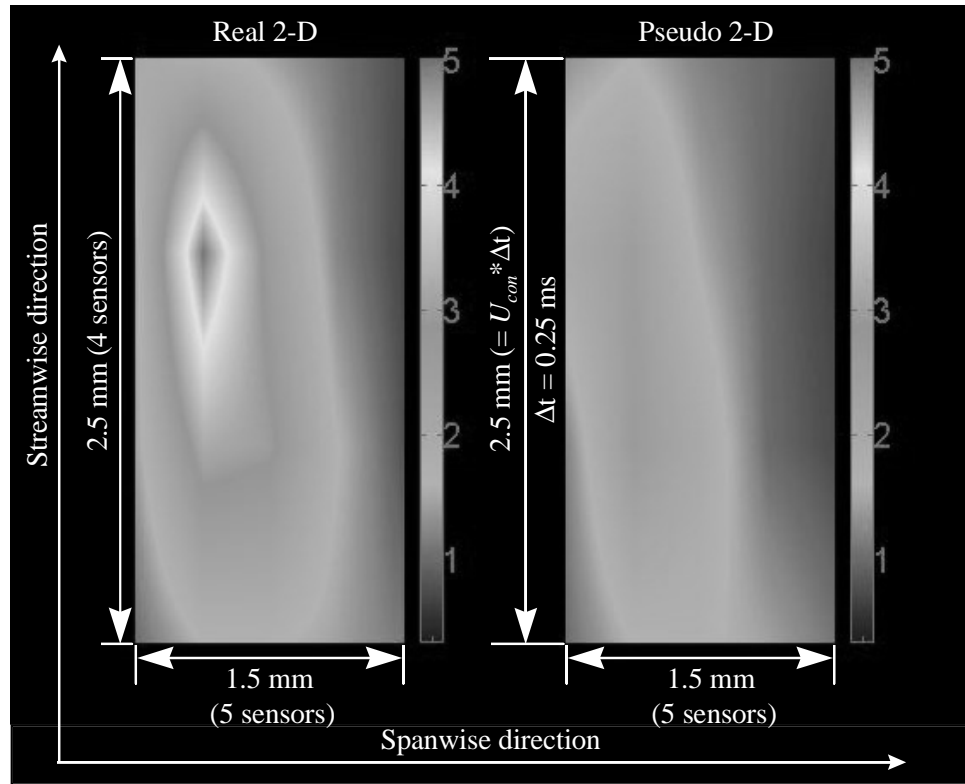
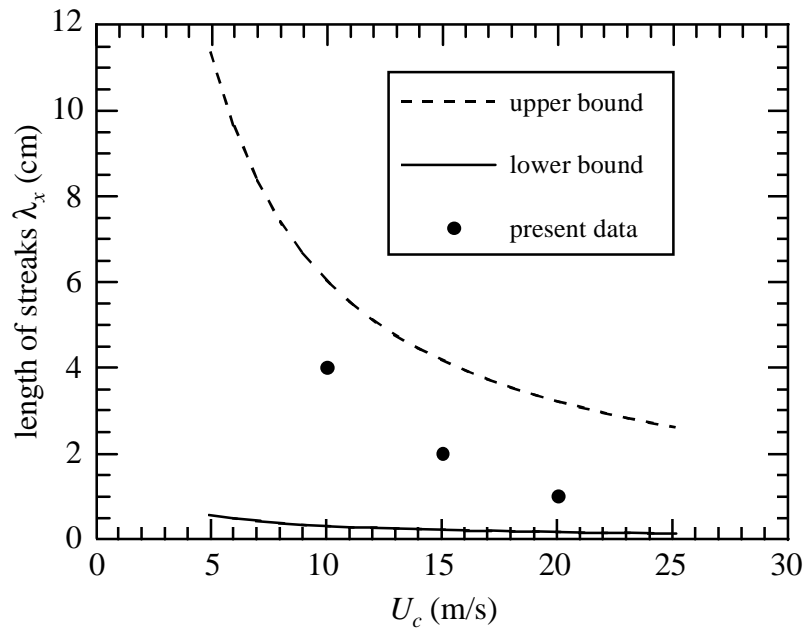
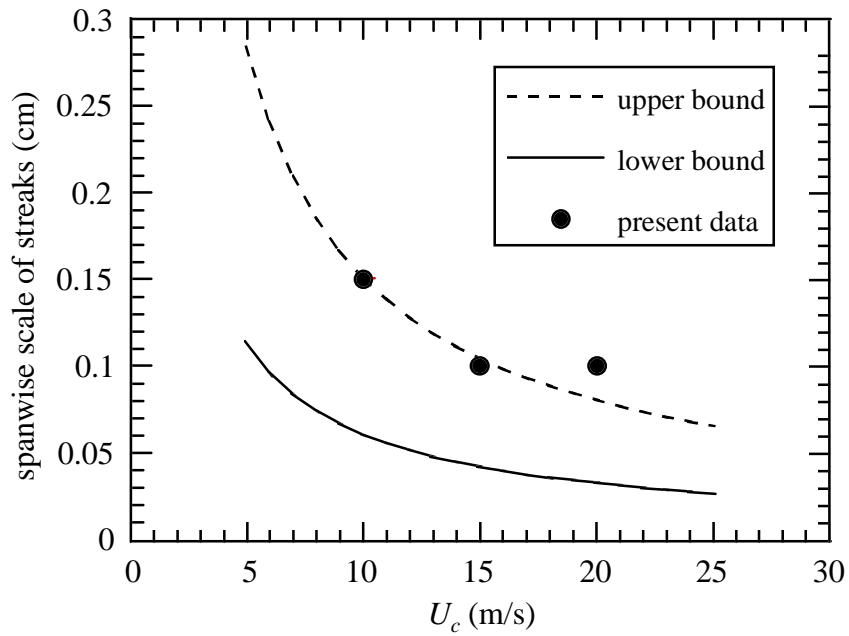


Figure 4.12 Comparison of the contour plots obtained by using 4 rows of sensors (real 2-D imaging) and by using only one row of sensors (pseudo 2-D imaging) at a centerline velocity of 20 m/s.

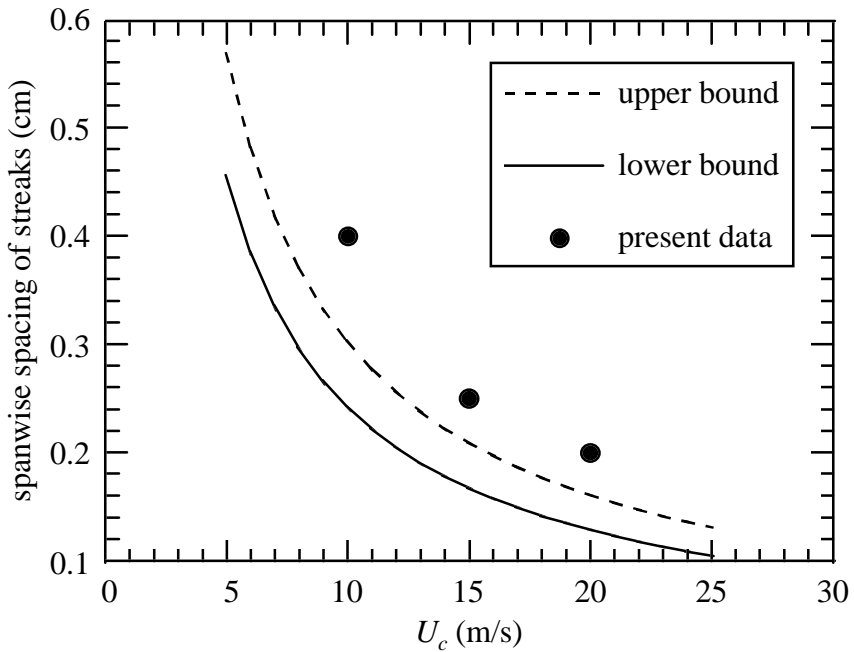
The contour plots in Figure 4.11 indicate that the scales of the streaks are different at different centerline velocities. The streaks in the high-speed (20 m/s) case appear to be thinner and more densely packed than those in the low-speed (8 m/s) case. Similar phenomena have also been observed in previous experiments. Based on real-time movies generated from the contour plots similar to the ones in Figure 4.11, the average streamwise length, the average spanwise scale, and the average spanwise spacing of the streaks at three different centerline velocities are estimated and shown in Figure 4.13. Once again, the present results agree well with previous studies. The average length of the present streaks falls within the upper and lower bounds of the established results. The average spanwise scale and spacing of the present streaks are either on or slightly higher than the upper bound.



(a) The length of streaks.



(b) The spanwise scale of streaks.



(c) The spanwise spacing of streaks.

Figure 4.13 Scales of the near-wall streaky structures at different Reynolds numbers.

4.5 Underwater Measurement

A shear stress sensor or hot-film sensor can be directly used in other electrically non-conductive fluid flows such as polymer. However, for underwater application, the leads or the entire sensor have to be coated with a layer of waterproof material for protection and electrical insulation purpose because water, especially sea water, is corrosive to metals and electrically conducting. The most commonly used coating material for conventional underwater hot-film sensors is thin (1-2 μm) quartz. It has been found that these quartz-coated hot-film sensors have serious drift problem during underwater measurement [19,20], even though they are operated at very low over-heat ratio to avoid bubble formation. The main reason is probe contamination in dirty water such as gradual build up of scale, algae, and minerals on the probe, causing a shift in the calibration. The other possibility might be that the surface of the conventional hot-film sensors before coating are rough and thin quartz coating can not cover the surface very well. Also, the sputtered quartz may not have good quality.

The coating materials for our MEMS shear stress sensors can be LPCVD silicon dioxide, PECVD silicon nitride or some organic materials such as Teflon and parylene. Among them, silicon nitride and Teflon are the best because nitride is resistant to sodium ion diffusion and Teflon is completely hydrophobic. Unfortunately, the first PECVD nitride deposition did not have good quality and spin-on Teflon did not have good adhesion to the sensor surface. As a result, only the LPCVD silicon dioxide has been successfully deposited on a shear stress imager wafer. The 2 μm thick oxide is patterned by photolithography and pad-etching to expose the bonding pads.

The packaging of the imaging chip for underwater measurement is shown in Figure 4.14. Epoxy is used to protect and insulate the bonding pads, bonding wires and soldering pads. As a result, the front surface is flat except the two bumps of epoxy on the edges of the imaging chip, which is acceptable for a demonstration and for drift testing only.

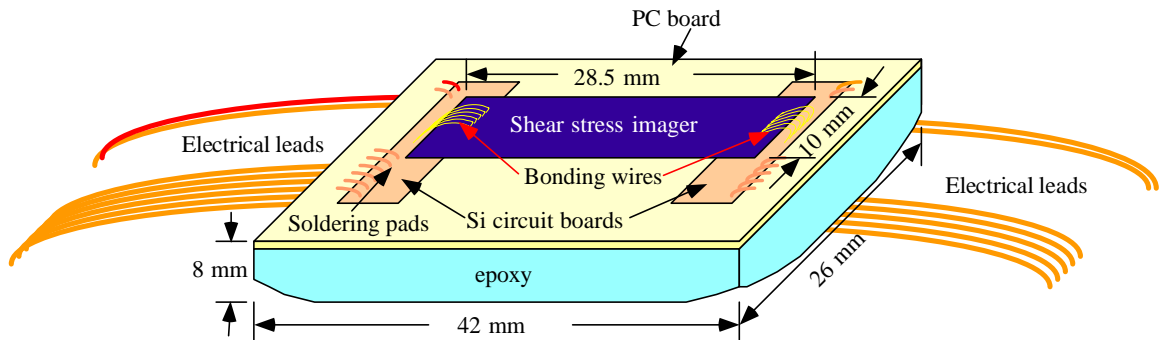


Figure 4.14 Schematic drawing of the packaging for underwater shear stress imager.

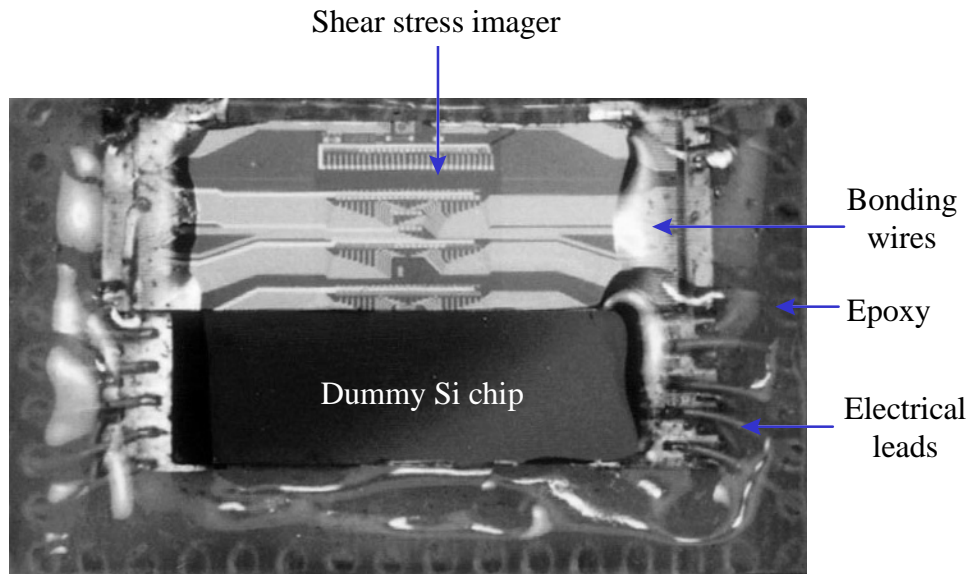


Figure 4.15 Photograph of the packaged shear stress imager for underwater measurement. Note that the imager is not diced in the same way as that in Figure 4.3 and the surface surrounding the imager and the dummy Si chip is not flat because of the hand-painted epoxy.

As usual, the sensors are biased in CT mode using the temperature compensated circuit in Figure 4.6. The over-heat ratio is only a few percent to avoid the bubble formation [21]. It has been found that the temporal drift of the sensor output voltage in water flow is very small (a few percent in 24 hours), probably because the sensor surface is smooth and the silicon dioxide deposited at 450°C has much better quality than the sputtered quartz. Due to the lack of shear stress information in the water channel used for

the testing, we could only calibrate the sensor against the free-stream speed (Figure 4.16). One catch of the instantaneous output voltage fluctuation is shown in Figure 4.17.

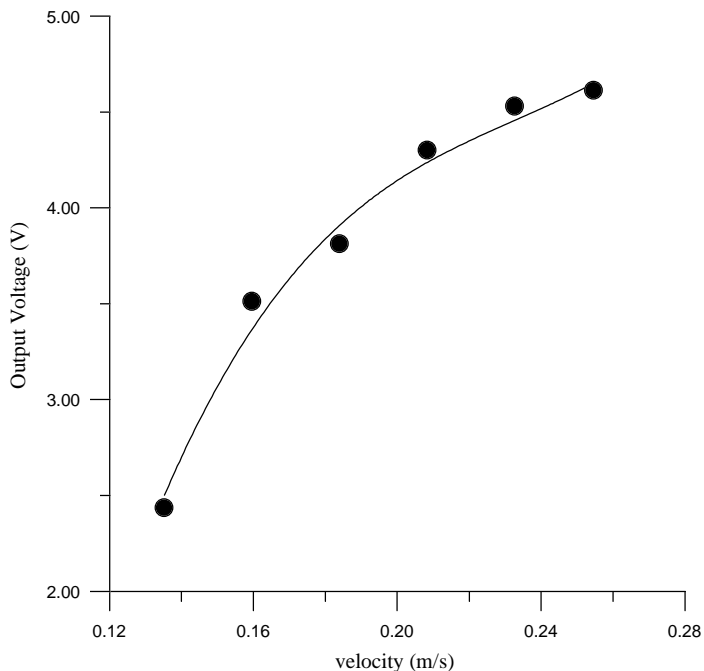


Figure 4.16 Calibration results of a shear stress sensor in a water channel.

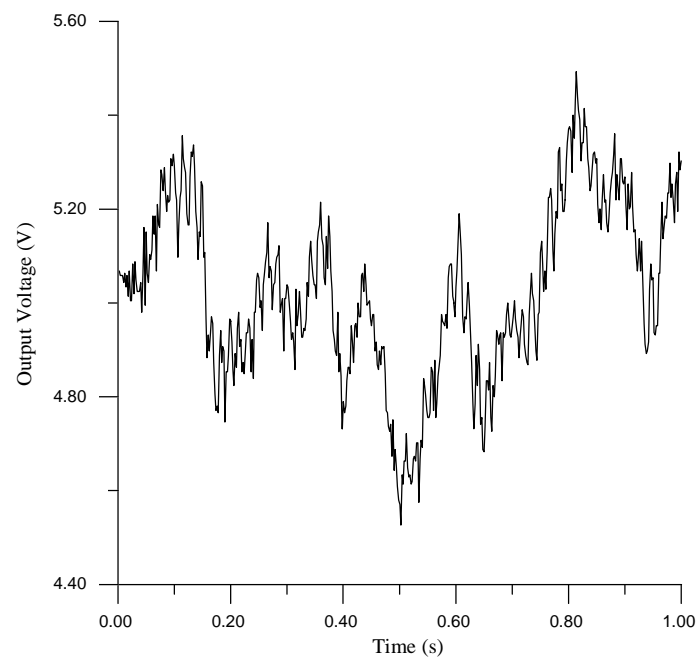


Figure 4.17 Instantaneous output voltage at a mean water flow speed of 25 cm/s.

The above preliminary study has only shown that the shear stress imager is potentially useful in underwater measurement. More work needs to be done, including better packaging and extensive steady-state and dynamic testing and analysis.

4.6 Summary

A new MEMS shear stress imager has been developed. More than 100 shear stress sensors are integrated on a $1 \times 2.85 \text{ cm}^2$ Si chip. Real-time 2-D shear stress imaging in air flow has been experimentally realized for the first time by using this imaging chip. The comparison between the measured results in a fully developed 2-D channel flow and other researchers' experimental and theoretical estimation has validated the use of the imager. Its potential application includes the study and control of turbulent air flows and even water flows, if the chip is coated with a layer of waterproof material, such as silicon dioxide.

The current packaging schemes for the imaging chip in air and water flow are not ideal as it has bonding wires sticking out from the surface which more or less interfere with the flow. However, this problem can be solved by improving the design such as using buried contacts, backside contacts or the MEMS skin technology that will be described in Chapter 6.

Bibliography

- [1] P. R. Bandyopadhyay, "Development of a Microfabricated Surface for Turbulence Diagnostics and Control," *ASME Application of Microfabrication to Fluid Mechanics*, Chicago, pp. 67-74, 1994.
- [2] D. M. Bushnell, "Turbulent Drag Reduction for External flows," AIAA Paper 83-0227, 1983.
- [3] P. Moin, J. Kim, and H. Choi, "On the Active Control of Wall-Bounded Turbulent Flows," AIAA Paper 89-0960, 1989.
- [4] A. K. M. F. Hussain and W. C. Reynolds, "The Mechanics of a Perturbation Wave in Turbulent Shear Flow," AFOSR Scientific Report 70-1655TR, 1970.
- [5] J. Cantwell, "Organized Motion in Turbulent Flow," *Ann. Rev. of Fluid Mech.*, Vol. 13, pp. 475-515, 1981.
- [6] C. M. Ho and P. Huerre, "Perturbed Free Shear Layers," *Ann. Rev. Fluid Mech.*, Vol. 16, pp. 365-424, 1984.
- [7] S. K. Robinson, "Coherent Motion in the Turbulent Boundary Layer," *Ann. Rev. Fluid Mech.*, Vol. 23, pp. 601-639, 1991.
- [8] J. C. Wyngaard, "Measurement of Small-Scale Turbulence Structure with Hot Wires," *J. Phys. E: Sci. Instr.*, Vol. 1, pp. 1105-1108, 1968.
- [9] R. F. Blackwelder, H. Eckelmann, "Streamwise Vortices Associated with the Bursting Phenomenon," *J. Fluid Mech.*, Vol. 94, pp. 577-594, 1979.
- [10] A. K. Praturi, R. S. Brodkey, "A Stereoscopic Visual Study of Coherent Structures in Turbulent Shear Flow," *J. Fluid Mech.*, Vol. 89, pp. 251-272, 1978.
- [11] S. J. Kline, W. C. Reynolds, F. A. Schraub, and P. W. Runstadler, "The Structure of Turbulent Boundary Layers," *J. Fluid Mech.*, Vol. 30, pp. 741-773, 1967.
- [12] H. P. Bakewell and J. L. Lumley, "Viscous Sublayer and Adjacent Region in Turbulent Pipe Flow," *Phys. Fluids*, Vol. 10, pp. 1880-1889, 1967.

- [13] L. S. G. Kovasznay, V. Kibens, and R. S. Blackwelder, "Large Scale Motion of Intermittent Region of a Turbulent Boundary Layer," *J. Fluid Mech.*, Vol. 41, pp. 283-325, 1970.
- [14] H. T. Kim, S. J. Kline, and W. C. Reynolds, "The Production of the Wall Region in Turbulent Flow," *J. Fluid Mech.*, Vol. 50, pp. 133-160, 1971.
- [15] T. J. Hanratty, L. G. Chorn, and D. T. Hatzivramidis, "Turbulent Fluctuations in the Viscous Wall Region of Newtonian and Drag Reducing Fluids," *Phys. Fluids*, Vol. 20 (10), pp. 112-119, 1977.
- [16] P. H. Ferredoxin, A. V. Johansson, J. H. Haritonidis and H. Eckelman, "The Fluctuating Wall-Shear Stress and the Velocity Field in the Viscous Sublayer," *Phys. Fluids*, Vol. 31, pp.1026-1033, 1988.
- [17] S. Obi, K. Inoue, T. Furukawa, and S. Masuda, "Experimental Study on the Statistics of Wall Shear Stress in Turbulent Channel Flows," *Tenth symposium on turbulent shear flows*, The Pennsylvania State University, Vol. 1, pp. 5-19 - 5-24, 1995.
- [18] J. Kim, P. Moin and R. Moser, "Turbulence Statistics in Fully Developed Channel Flow at Low Reynolds Number," *J. Fluid Mech.*, Vol. 177, pp. 133-166, 1987.
- [19] F. J. Resch, "Hot-Film Turbulence Measurements in Water Flows," *J. Hydr. Div. ASCE*, Vol. 96, No. HY3, pp. 787-800, 1970.
- [20] K. A. Warschauer, J. B. A. Vijge, and G. A. Boschloo, "Some Experiences and Considerations on Measuring Turbulence in Water with Hot Films," *Appl. Sci. Res.*, Vol. 29, pp. 81-98, 1974.
- [21] C. G. Rasmussen, "The Air Bubble Problem in Water Flow Hot-Film Anemometry," *DISA Info.*, No. 5, pp. 21-26, 1967.